https://doi.org/10.5194/egusphere-2026-485
Preprint. Discussion started: 13 February 2026

Comparing high spatial and temporal resolution snow depth measurements and modelling results in an avalanche release area

Pia Ruttner[1,2,3], Nora Helbig[1,4], Annelies Voordendag[3], Andreas Wieser[3], and Yves Bühler[1,2]

[1]WSL Institute for Snow and Avalanche Research SLF, Davos Dorf, 7260, Switzerland
[2]Climate Change, Extremes, and Natural Hazards in Alpine Regions Research Center CERC, Davos Dorf, 7260, Switzerland
[3]Institute of Geodesy and Photogrammetry, ETH Zurich, Zurich, 8092, Switzerland
[4]Eastern Switzerland University of Applied Sciences, Rapperswil, Switzerland

Correspondence: Pia Ruttner (pia.ruttner@slf.ch)

Abstract.

Accurate representation of snow depth distribution within avalanche release areas is critical for understanding avalanche formation and supporting operational avalanche mitigation measures. In this study, we investigate the spatial variability of snow depth in an avalanche release area using high spatial (0.5 m) and temporal (hourly) resolution measurements obtained from a low-cost terrestrial laser scanner (TLS). The TLS data provide detailed snow depth distributions for three selected snow accumulation events, including sub-event evolution, enabling an event- and sub-event-based analysis of snow deposition patterns.

We assess the ability of three terrain-based modelling approaches to reproduce observed snow depth patterns: the topographic position index (TPI), a wind shelter index (Sx), and a statistical preferential deposition model. The results indicate that simple topography-derived indices generally achieve the highest correlations with measured snow depths across most events. The correlations reach maximum values of up to 0.57 (Spearman correlation), indicating that topographic predictors are able to partially, but not fully explain the present snow depth variability at sub-metre spatial resolution.

These findings emphasise the dominant role of local terrain in shaping snow accumulation patterns within avalanche release areas, demonstrate the value of TLS data for event-scale model evaluation, and highlight the potential to complement incomplete observations using simple terrain-based modelling approaches. The collection of additional snow depth distribution data with such high spatio-temporal resolution in different avalanche release areas would enable the development of machine learning approaches in the future. This fosters event-based avalanche forecasting by improving the spatial completeness of snow depth observations in complex terrain at slope scale.

1 Introduction

The spatial variability of snow depth across a slope is determined by several processes. A key factor is wind, leading to preferential deposition during snowfall events from the interaction of snow particles with topography and wind (Föhn and Meister, 1983; Lehning et al., 2008). After that, when the wind speeds exceed the threshold friction velocity (Li and Pomeroy, 1997),

https://doi.org/10.5194/egusphere-2026-485
Preprint. Discussion started: 13 February 2026

it leads to substantial snow redistribution (Lehning and Fierz, 2008; Li et al., 2018) as well as to drifting snow sublimation (Groot Zwaaftink et al., 2013). Wind loading, which commonly occurs on lee slopes during windy conditions, is a major contributor to avalanches by forming wind slabs over a soft and weak layer (Schweizer et al., 2003). Therefore, accurate knowledge of the spatial snow depth distribution, especially in avalanche release areas, is crucial for risk based decision making, as for remote avalanche control systems or temporary road closures.

Automated snow measurements in mountainous terrain are typically located in flat areas (flat field stations). However, such point-wise observations have been shown to be unrepresentative for mean snow conditions in the surrounding terrain (Grünewald and Lehning, 2015). Furthermore, spatial snow depth variability increases considerably as the spatial scale decreases from a few square kilometers to meter-scale areas (Melvold and Skaugen, 2013; Grünewald et al., 2013; Helbig et al., 2015). For an accurate representation of spatial snow depth variability in terrain prone to avalanches, measurements with high spatial resolution (sub-meter) are inevitable. The most established approaches for this purpose include terrestrial laser scanning TLS (Prokop, 2008; Grünewald et al., 2010; Schirmer et al., 2011; Deems et al., 2013; Adams et al., 2013; Revuelto et al., 2014; Deems et al., 2015; Voordendag et al., 2024) and aerial photogrammetry (Bühler et al., 2015; Vander Jagt et al., 2015; Nolan et al., 2015; Bührle et al., 2023; Meyer et al., 2022). These approaches require high logistical and financial effort, typically rely on suitable meteorological conditions (Bühler et al., 2016), and are thus often limited to a few acquisitions per winter season. To overcome this, research groups have recently started exploring the potential of permanently installed low-cost systems (Ruttner et al., 2025; Goelles et al., 2025).

In most regions observations from avalanche release areas in real time and with high spatial resolution are not available. Even in places where for example lidar sensors are installed, it is likely that they fail to provide meaningful data during periods of fog or strong snowfall. Thus, in the absence of spatial observations or when data are missing, a modelled spatial snow depth distribution can provide valuable information.

Spatial snow depth patterns are strongly controlled by terrain characteristics, and numerous studies have quantified these relationships across a range of spatial scales. Spatial mean snow depth and snow depth variability has been linked to terrain descriptors including elevation, slope angle, curvature, aspect, local surface roughness, terrain correlation length, and upwind sheltering angle (Winstral et al., 2002; Grünewald et al., 2010; Schirmer et al., 2011; Lehning et al., 2011; Skaugen, 2007; Grünewald et al., 2013; Melvold and Skaugen, 2013; Helbig et al., 2015; Grünewald and Lehning, 2015; López-Moreno et al., 2017; Skaugen and Melvold, 2019; Revuelto et al., 2020a; Helbig et al., 2021; Boardman et al., 2025; Schön et al., 2015).

Complex atmospheric snow-transport models explicitly resolve the interaction between wind, snow particles, and terrain, including processes such as saltation, suspension, deposition, and erosion (Liston and Sturm, 1998; Gauer, 2001; Schneiderbauer and Prokop, 2011; Hames et al., 2022; Wang and Huang, 2017; Aksamit et al., 2025; Li et al., 2018; Gerber et al., 2017; Vionnet et al., 2014; Saigger et al., 2024). Models that couple physical snow processes to detailed snowpack schemes, such as Alpine3D (Lehning et al., 2006) or SnowPappus (Baron et al., 2023), are designed for snow cover simulations that can cover large domains and are in part also in operational use. However, these approaches require substantial computational resources and comprehensive wind field data, which restricts either the spatial extent, the temporal extent, and the spatio-temporal resolution of the modelling.

https://doi.org/10.5194/egusphere-2026-485
Preprint. Discussion started: 13 February 2026

To balance physical realism and computational efficiency, several models with intermediate-complexity have been proposed. These approaches simplify certain transport processes while retaining essential dynamics of wind-driven snow redistribution, enabling larger domains or longer simulation periods at manageable computational cost (Vionnet et al., 2021; Quéno et al., 2024). Lower-complexity models, such as statistical models, relate terrain and meteorological parameters to snow depth patterns (Grünewald et al., 2013; Meloche et al., 2022; Revuelto et al., 2020b; Daudt et al., 2023; Helbig et al., 2024). These data-driven methods offer attractive alternatives, but when trained on data from a single region, they risk regional overfitting (Revuelto et al., 2020b).

Despite substantial progress in modelling spatial snow depth variability, important limitations remain, particularly in the steep slopes of avalanche release areas. Most existing studies focus on a basin-scale, with resolutions of 10-100 m, while investigations at sub-metre spatial resolution are rare. Although some research analysed individual snowfall events using terrain-based parameters (Schön et al., 2015; Prokop et al., 2013), the temporal gaps between snowfall and measurement often span several days, during which additional processes such as settling and melt may alter the snow depth distribution. As a result, the isolated effect of wind-driven deposition remains difficult to assess.

In this study we compare observations of changes of snow depth (ΔHS) at high spatio-temporal resolution, with ΔHS derived from terrain and wind-exposure indices, and a statistical downscaling model for preferential deposition. We assess how the predicted ΔHS change when using different data sources for the wind speed and wind direction, and when using a digital surface model (DSM) representing the snow-covered surface instead of the terrain without snow. Furthermore, we are exploring the applicability of these models to fill in spatial gaps in our measurement data, which are related to weather conditions or terrain shadowing due to the setup geometry.

2 Data

2.1 Terrestrial laser scanning (TLS) data

This study uses snow depth data from two permanent low-cost terrestrial laser scanning stations (B1 and B2) at the testsite Braemabuel, in Dischma valley, close to Davos in Switzerland, see Fig. 1. At each of these stations, we operate a Livox Avia lidar sensor. Jointly, these sensors cover the release area of the Wildi-avalanche. The lidar sensors measure at a wavelength of 905 nm which is optimal for sensing snow (Wiscombe and Warren, 1980; Prokop, 2008). We installed the sensors on 23 November 2023 and configured them to scan every hour. The specified maximum measurement range of the lidar sensors is 450 m, but in our region of interest we achieve around 150 m, due to the suboptimal measurement geometry. The data cover an area of about $14\,500\,\mathrm{m}^2$, with an average resolution of 0.1 m. Accounting for measurement accuracy, registration errors and rasterization/interpolation errors the data has an accuracy of 0.1–0.3 m. We processed the data to a gridded raster data of 0.5 m resolution. A more detailed description of the sensors, setup, data processing, and data quality is given in Ruttner et al. (2025).

https://doi.org/10.5194/egusphere-2026-485
Preprint. Discussion started: 13 February 2026

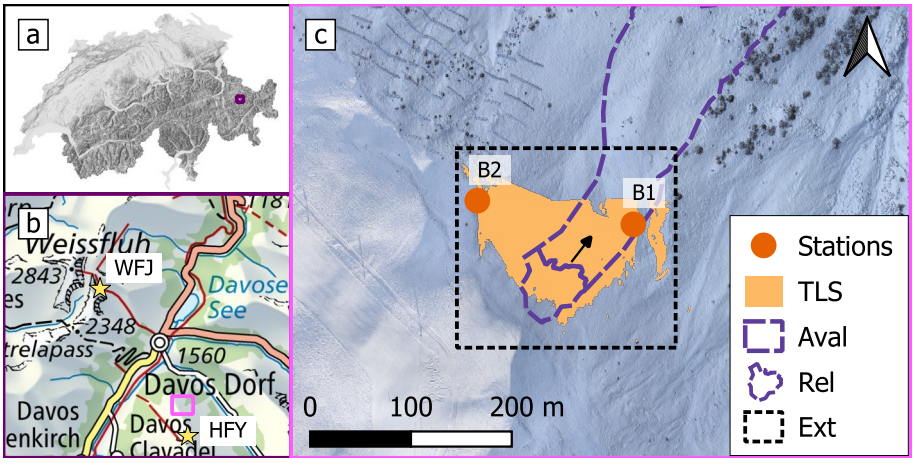

Figure 1. Overview of the study area Braemabuel (a) within in Switzerland, (b) near Davos and the two weather stations Weissfluhjoch (WFJ) and Holfuy Braemabuel (HFY), and (c) the locations of the measurement stations, the area covered by the terrestrial lidar scans (TLS), outline (Aval) and release area (Rel) of the Wildi avalanche in 2019, and the extent used for modelling changes of snow depth (Ext, 217×198m). The arrow indicates the flow direction of the avalanche. The background image is an orthophoto derived from the photogrammetric drone flight on 12 December 2023. (map source: Federal Office of Topography)

2.2 Meteorological data

Across the approaches for modelling snow depth distribution in our study, we use wind direction, wind speed, precipitation amount and snow density data. To ensure the robustness and applicability of our approaches, we primarily rely on data from numerical weather prediction models, which offer greater consistency and coverage compared to station-based measurements. We use the Kenda-CH1 analysis data of the ICOsahedral Non-hydrostatic (ICON) modelling framework (Zängl et al., 2015), which contain, amongst many other variables, precipitation, wind speed and wind direction on a 1.0 km grid, at 10 m above ground, in Switzerland. We use the hourly values of the grid cell, whose centre is closest to our study site. The closest measurement station at similar altitude, where all information is available to derive snow density, is at Weissfluhjoch (WFJ), located about 5.5 km from our test site Braemabuel (see Fig. 1b). At WFJ researchers measure the height and water equivalent of new snow (HN and HNW) on a daily basis, from which we derive the density of new snow.

Furthermore, we use wind data from local weather stations to compare model performance when using either data from local measurement stations or gridded meteorological data. This comparison allows us to assess how sensitive the model is to the choice of data source. Close to our test area are three weather stations that measure, among other parameters, wind speed and wind direction: Our TLS measurement stations B1, B2 (see Fig. 1c) and the privately owned weather station holfuy HFY on top of the close-by peak (500 m horizontal, and 200 m vertical distance, see Fig. 1b). The data of the latter is accessible through the platform *holfuy* (Holfuy, 2025).

https://doi.org/10.5194/egusphere-2026-485
Preprint. Discussion started: 13 February 2026

2.3 Terrain models

The terrain data used in this study are digital surface models (DSMs), derived from photogrammetric drone flights with a Wingtra One Gen II fixed-wing UAV using a Sony DSC-RX1RM2 42 megapixel camera and Post Processing Kinematics (PPK) postitioning. We processed the photogrammetric data as described in Bühler et al. (2016), Adams et al. (2018), and Eberhard et al. (2021) using the software Agisoft Metashape Professional, Version 1.6.5. We use the DSM acquired on 18 October 2022, as snow-off reference, and one from 19 December 2023, which is a DSM of the snow-covered terrain. The DSMs have a spatial resolution of 0.1 m, and we downsample them to 0.5 m to meet the resolution of the TLS data.

2.4 Selected meteorological events

The available TLS data cover the two winter seasons 2023/2024 and 2024/2025. The former had exceptionally high snow depths and a generally stable snowpack in the area of Davos (Pielmeier et al., 2024). The 2024/2025 season, on the other hand, was characterised by very little snow. We thus focus on the winter 2023/2024 in this paper. We identified 15 potentially interesting events with a significant amount of new snow (defined as more than 0.1 m from start to end of the event), in that season. For the selection of TLS measurement epochs, we use the the number of classified ground points per scan as proxy for snowfall in the monitored area, with the assumption that less ground points, mean heavier snowfall (note that some epochs are missing from station B2 due to sensor outages, and some from station B1 due to the scanner being snow covered). We were looking for rather short events with TLS measurements available directly before and after, so we can assume that processes other than snowfall and wind-driven redistribution, e.g., settlement or melting, have little influence on snow depth changes during the events. Among those, we selected the events without avalanche activity but with continuous availability of locally collected meteorological data (wind sensor not frozen).

With all these criteria applied, three events stand out. We indicate them as E1, E2, and E3, and analyse them, herein. More precisely, the evaluated periods are E1: 24 November 2023 14:00 UTC – 26 November 2023 08:00 UTC, E2: 21 December 2023 09:00 UTC – 23 December 2023 03:00 UTC and E3: 22 February 2024 22:00 UTC – 23 February 2024 16:00 UTC. They are distributed over the winter season and show a variety in average wind speed. With the latter we expect the presence of different processes per event (mainly preferential deposition and snow redistribution), for which we want to specifically evaluate the models. Figure 2 gives an overview of the selected events.

Due to the varying wind speeds and directions, we further divide the events into sub-events. There, we rely on the availability of suitable lidar data (i.e. epochs which cover more than half of the test site). According to the available lidar data and best possible consideration of wind speeds and wind direction, we use the TLS acquisitions of 25 November 2023 02:00 UTC and 10:00 UTC during E1 and 21 December 2023 19:00 UTC, 22 December 2023 03:00 UTC and 09:00 UTC during E2 (also see orange, vertical lines in Fig. 2). We do not have suitable lidar scans to further sub-divide E3, therefore we use only the full event herein.

During the event in November 2023 (E1) the ICON model outputs an accumulated precipitation of 27.9 mm and average wind speeds of 5.7 m/s, mainly from north-west. At measurement station B1, which is located in the slope of interest, we

https://doi.org/10.5194/egusphere-2026-485
Preprint. Discussion started: 13 February 2026

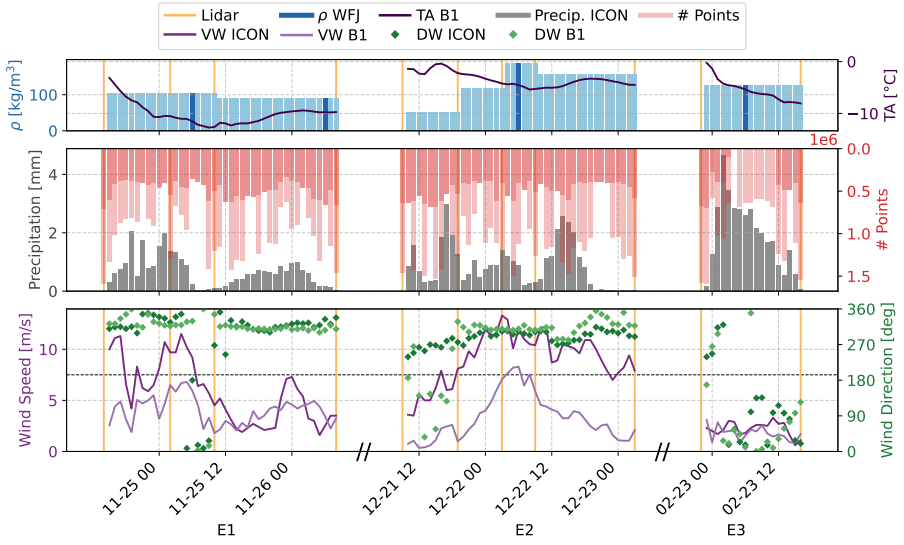

Figure 2. Meteorological conditions during the selected events. The orange vertical lines indicate the times of the lidar measurements we use in this study. The measured density of new snow ρ WFJ is shown in dark blue, and in light blue we show the exact values we use for each event and sub-event. TA B1 is the air temperature, measured at station B1. The precipitation values correspond to the 1 hour accumulated precipitation as snowfall from the ICON dataset. The # points is the number of valid points per epoch, darker red is the point count from station B1, stacked with lighter red for the point count from station B2. For the wind direction (DW) and wind speed (VW) we show the 1 hour mean values of the ICON dataset and of the measurement station B1. For orientation, we enhanced the grid line at 7.5 m/s, which is the mean threshold for snow redistribution.

recorded an average wind speed of 4.0 m/s and gusts of maximum 11.2 m/s. Station B2, which is on the local ridge, and HFY, located at the local peak, (see Fig. 1), measured higher values (Tab. 1). The threshold for snow transport is 4–11 m/s for dry snow, with an average of 7.5 m/s for fresh snow (Li and Pomeroy, 1997). However, this threshold depends on many factors beyond wind speed, in particular on snow surface properties. Based on the locally measured wind speeds and evaluation of the differences of the TLS scans, we assume that during the event a mix of preferential deposition and snow redistribution lead to the variability of new snow depths in E1. With further dividing the event into sub-events, we assume the first hours where a mix of preferential deposition and redistribution, followed by a few hours of snow redistribution and then a period of preferential deposition in the second half of the event (see Tab. 1). In the event in December 2023 (E2) we retrieve an accumulated precipitation of 36.6 mm from the ICON model and an average wind speed of 9.1 m/s, from west- and north-west directions. During the first hours of the event we recorded low wind speeds of 1–3 m/s (B1), with rather warm temperatures (while below zero). After that, the wind speeds picked up and there were a few hours with high wind speeds, on average 9.3 m/s and gusts up to 18.8 m/s (referring to station B1). From this we assume that there was a rather homogeneous accumulation with preferential deposition of new snow in the beginning (although due to the warmer temperatures most likely including other processes like settlement as well), which was afterwards transported and redistributed, at the same time combined with

https://doi.org/10.5194/egusphere-2026-485
Preprint. Discussion started: 13 February 2026

more new snow. We classify this event as well as a mixture of mainly preferential deposition and snow redistribution, with sub-events of mixed processes, redistribution and preferential deposition (also see Tab. 1). During the event in February 2024 (E3), the accumulated precipitation was 34.6 mm and the average wind speed reached 3.3 m/s with great variation in wind directions, according to the ICON model. As the wind speeds recorded within the slope (on average 3.4 m/s) are below the reported threshold for snow transport, we assume that there was no snow redistribution, but preferential deposition of the new snow.

Table 1. Mean and maximum wind speeds for each event and sub-event, measured at stations B1, B2, HFY and retrieved from the ICON model, as well as the accumulated water equivalent of new snow (HNW) and our event type classification.

	VW mean [m/s]				VW max [m/s]			HNW	Event type
	B1	B2	HFY	ICON	B1	B2	HFY	[mm]	
E1	4.0	5.2	4.9	5.7	12.4	19.8	23.9	27.9	Mix
11-24 14 - 11-25 02	4.3	4.8	8.0	8.2	11.2	15.1	23.9	13.4	Mix
11-25 02 - 11-25 10	4.7	5.7	6.0	8.0	12.4	16.9	17.5	3.8	Redistribution
11-25 10 - 11-26 08	3.6	5.4	2.9	3.6	9.1	19.8	8.6	10.7	Pref. dep.
E2	3.2	4.6	6.5	9.1	18.8	23.9	23.1	36.5	Mix
12-21 09 - 12-21 19	1.3	3.1	7.8	5.7	8.1	9.8	20.6	12.1	Mix
12-21 19 - 12-22 03	4.0	5.3	7.9	10.8	12.1	18.2	21.9	6.4	Mix
12-22 03 - 12-22 09	7.3	8.5	9.8	11.1	18.8	23.9	23.1	3.9	Redistribution
12-22 09 - 12-23 03	2.8	3.7	4.1	9.5	8.8	14.4	15.3	14.1	Pref. dep.
E3	1.8	3.3	3.7	2.2	5.4	9.1	13.1	34.4	Pref. dep.

3 Methodology

To compare the TLS measurements to the model results, we calculate snow depths with all models on the spatial extent of the rectangle 'Ext' shown in Fig. 1, at 0.5 m resolution. All comparisons to TLS measured change of snow depth (HN), are performed only on the pixels where TLS measurements are available (individual mask per event).

3.1 Terrain-dependent indicators

Snow depth distribution at small scale closely follows the local terrain. Usually, there are larger snow depths in gullies and depressions than on ridges and hilltops. We use two terrain-dependent parameters that have been widely used to model snow depth distribution.

https://doi.org/10.5194/egusphere-2026-485
Preprint. Discussion started: 13 February 2026

3.1.1 Topographic position index TPI

The topographic position index TPI (Weiss, 2001) describes the relative elevation of a point, compared to the mean elevation of the surrounding terrain, in an application-specific radius. This allows the use of TPI to indicate slope positions and landforms, such as depressions, plains or ridges and hilltops. Depending on the selected radius, different scales of topography are described (Weiss, 2001). The TPI is calculated as follows:

$$\mathrm{TPI}_j^R = z_j - \bar{z}_j^R \tag{1}$$

where j is the index of the point for which the TPI is evaluated, z_j is its elevation vertical coordinate, and $\bar{z}_j^R$ is the average elevation of all points within a circle of radius R around point j. For simplicity, we will subsequently omit the superscript R, herein.

Positive values for TPI indicate ridges and hilltops, whereas negative values imply landforms such as gullies and depressions, suggesting a negative correlation with snow depths. In Sec. 3.1.4 we describe our derivation of height of new snow HN from TPI.

3.1.2 Wind shelter index Sx

Snow depth distribution is dependent not only on the local terrain geometry, but also on the wind direction. Snow gets eroded on the windward side, and then deposits on the leeward side of a ridge. Winstral et al. (2002) developed an indicator, whether a cell is wind exposed or wind sheltered, by evaluating the terrain elevation of a cell in relation to terrain elevations of all cells in a certain wind direction and up to a user-specified distance. Whether the elevation along the assessed wind direction is higher or lower than the elevation at the point of interest provides a basic approximation of whether it is exposed or sheltered from the wind in this direction, which we assume to be positively correlated to snow depths (see Sec. 3.1.4 for derivation of HN from wind shelter index Sx).

The windshelter index Sx of a cell $\mathbf{X}_j(x_j, y_j, z_j)$ describes the maximum upward slope of all cells $\mathbf{X}_d(x_d, y_d, z_d)$, along an azimuth angle A, and a maximum search distance D with:

$$Sx_j^{A,D} = \max\left[\arctan\left(\frac{z_d - z_j}{\sqrt{(x_d - x_j)^2 + (y_d - y_j)^2}}\right)\right], \tag{2}$$

When taking into account a number of azimuths n_A, resulting from incrementing with a defined step size from A_1 to A_2, Sx can be extended to $\overline{Sx}$ by taking the mean of all Sx per cell j with:

$$\overline{Sx}_j^{A,D}\Big|_{A_1}^{A_2} = \frac{1}{n_A}\sum_{A=A_1}^{A_2} Sx_j^{A,D}, \tag{3}$$

We take the approach a step further and instead of equally weighting all considered wind directions in the above $\overline{\mathrm{Sx}}$, we compute a wind rose and calculate a weighted mean $\overline{\mathrm{Sx}}^w$, according to the relative occurrence of the observed wind directions within azimuth bins of specified angle width. This ensures that dominant wind directions get more weight and less frequent

https://doi.org/10.5194/egusphere-2026-485
Preprint. Discussion started: 13 February 2026

wind directions are taken into account, but are not over emphasised. In the remainder of the paper we use $\overline{\mathrm{Sx}}^{w}$ for our analysis, but use the notation Sx, for simplicity.

3.1.3 Parameter selection for TPI and Sx

We calculated the terrain indices Sx and TPI on the summer DSM, acquired by a photogrammetric drone on 18 October 2022. To find the optimal TPI radius R and Sx maximum search distance D for our application, we first calculated the Spearman correlations between the measured change of snow depth ΔHS (of each larger event E1, E2, and E3) and TPI and Sx, for a range of radii and distances (Fig. 3). The correlation varies depending on the event. For our analysis we choose $R = 10$ m for TPI and $D = 8$ m, as these are the mean of the best correlation values for E1 and E2, and use it for all computations. For the Sx computations we choose an angular step width of 5 deg and use hourly wind directions.

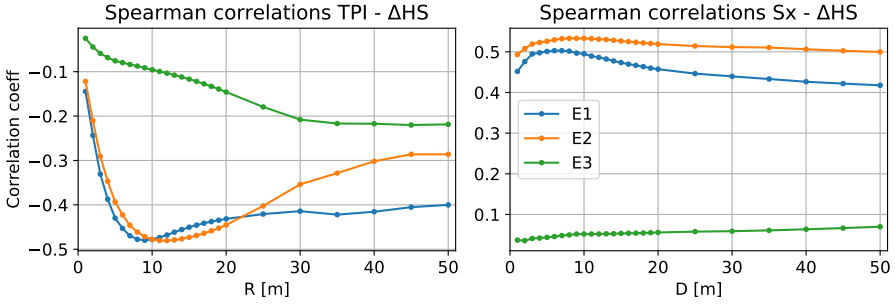

Figure 3. Spearman correlations between measured height of new snow HN (for E1, E2 and E3) and TPI and Sx, with varying radii R for TPI (left) and maximum search distance D for Sx (right).

3.1.4 Relation of TPI and Sx to snow depth

We take a mean water equivalent of new snow per cell $\overline{\mathrm{HNW}}$ and determine a factor, depending on TPI or Sx, to increase or decrease the amount of HNW relative to the mean value. In our study we use the same value of $\overline{\mathrm{HNW}}$ for each cell, which is the value of the closest ICON cell. Based on Winstral and Marks (2002), MeteoIO (Bavay and Egger, 2014) and Helbig et al. (2024) we determine HNW of a cell with index j, depending on its Sx value, which we scale by the mean μ and standard deviation σ, with:

$$\mathrm{HNW}_j^{\mathrm{Sx}} = \begin{cases} \overline{\mathrm{HNW}}\left(1 - \left|\frac{\mathrm{Sx}_j}{\mu_{\mathrm{Sx}} - \sigma_{\mathrm{Sx}}}\right|\right) & \text{if } \mathrm{Sx}_j < 0 \\ \overline{\mathrm{HNW}}\left(1 + \alpha\frac{\mathrm{Sx}_j}{\mu_{\mathrm{Sx}} + \sigma_{\mathrm{Sx}}}\right) & \text{if } \mathrm{Sx}_j > 0 \quad \text{with} \quad \alpha = \frac{\sum\left|\frac{\mathrm{Sx}_j}{\mu_{\mathrm{Sx}} - \sigma_{\mathrm{Sx}}}\right|}{\sum\frac{\mathrm{Sx}_j}{\mu_{\mathrm{Sx}} + \sigma_{\mathrm{Sx}}}} \end{cases} \tag{4}$$

In the above mentioned references Sx is scaled by its minimum (Sx<0) and maximum (Sx>0). We found the minimum and maximum to be very sensitive to the extent of the evaluated area, and therefore apply a different scaling in this study.

https://doi.org/10.5194/egusphere-2026-485
Preprint. Discussion started: 13 February 2026

We introduce the same principle for TPI, but we assume that areas with $TPI > 0$ are depleted and $TPI < 0$ are enriched (relative to $\overline{\text{HNW}}$):

$$\text{HNW}_j^{\text{TPI}} = \begin{cases} \overline{\text{HNW}} \left(1 - \frac{\text{TPI}_j}{\mu_{\text{TPI}} + \sigma_{\text{TPI}}}\right) & \text{if TPI}_j > 0 \\ \overline{\text{HNW}} \left(1 + \alpha \left| \frac{\text{TPI}_j}{\mu_{\text{TPI}} - \sigma_{\text{TPI}}} \right|\right) & \text{if TPI}_j < 0 \quad \text{with} \quad \alpha = \frac{\sum \frac{\text{TPI}_j}{\mu_{\text{TPI}} + \sigma_{\text{TPI}}}}{\sum \left| \frac{\text{TPI}_j}{\mu_{\text{TPI}} - \sigma_{\text{TPI}}} \right|} \end{cases} \tag{5}$$

We convert HNW to height of new snow HN, by using the temporal mean snow density $\overline{\rho}$ for each event E={E1, E2, E3} obtained from the WFJ observations (Fig. 1), which we assume to be constant over the evaluated area. The computed HN per pixel j and event E, derived from Sx, is therefore calculated with:

$$\text{HN}_{j,\text{E}}^{\text{Sx}} = \text{HNW}_{j,\text{E}}^{\text{Sx}} / \overline{\rho_{\text{E}}} \tag{6}$$

The same equation holds for $\text{HN}_{j,\text{E}}^{\text{TPI}}$, but using TPI to calculate $\text{HNW}_{j,\text{E}}^{\text{TPI}}$.

To be precise, the results of the scaling by mean and standard deviation are not HNW, since the values can become negative. Therefore, we refer to the model output using TPI and Sx, as change of snow depth ΔHS.

Figure 4 (top left) shows the resulting TPI. The relatively small radius of 10 metres reveals detailed slope structures showing local depressions and elevations. We calculate Sx in hourly time steps, scale each time step using the corresponding $\overline{\text{HNW}}$ from ICON, apply weighted means from 5 degree wind direction angular intervals, and then accumulate the results to the time intervals, as defined with the events. In Fig. 4 (top center) we show the Sx angles for an example epoch of f 25 November 2023 21:00 - 22:00 UTC, where the average wind direction was from 315 deg. In the bottom row of Fig. 4 are the scaled terrain parameters, using a $\overline{\text{HNW}}$ of 0.8 mm.

3.2 Preferential deposition from statistical snowfall downscaling PD

Helbig et al. (2024) developed a statistical snowfall downscaling scheme based on parameters derived from a comprehensive 30 m new snow database, generated using 3D atmospheric model wind simulations over synthetic topographies spanning a broad range of slope characteristics, together with a snow transport model to compute preferential deposition. This dataset describes how snowfall is non-uniformly deposited on the ground in mountainous terrain due to interactions between near-surface wind, snow particles, and topography. Processes such as snow erosion, saltation, drifting snow sublimation, and snow melt or settlement were intentionally suppressed and are therefore not represented in the PD model. The downscaled snowfall, or water equivalent of new snow per pixel HNW_j^{PD} is calculated by scaling $\overline{\text{HNW}}$ by a local downscaling factor $X_{\text{dsc},j}$:

$$\text{HNW}_j^{\text{PD}} = \overline{\text{HNW}}\, X_{\text{dsc},j} \tag{7}$$

$X_{\text{dsc},j}$ describes primarily the correlation of preferentially deposited snowfall with local vertical wind speed w_j (with updraft on the windward side of mountains and downdraft on the lee side), in line with earlier studies reporting correlations between

https://doi.org/10.5194/egusphere-2026-485
Preprint. Discussion started: 13 February 2026

vertical wind speed and preferential deposition (Lehning et al., 2008; Dadic et al., 2010). Helbig et al. (2024) further showed that preferential snowfall deposition scales with the local slope parameter μ_j ($\mu = \sqrt{((\partial_x z)^2 + (\partial_y z)^2)/2}$). $X_{\mathrm{dsc},j}$ is

$$X_{\mathrm{dsc},j}(w_j, \mu_j) = \mathrm{erfc}(\mathrm{a}\, w_j\, (w_j + |w_j|))^{\mathrm{b}}\, (1 - \mathrm{c}\, w_j + \mathrm{d}\, w_j^3)(1 + \mathrm{e}\, \mu_j^{\mathrm{f}}), \tag{8}$$

with the following constant values for a to f: a = 0.4825, b = 0.03418, c = 0.592003, d = 0.004452, e = 0.24714 and f = 2.24223. $X_{\mathrm{dsc},j}$ requires local vertical wind speed. When spatially fine-scale w is unavailable as in our case, Helbig et al. (2024) introduced a statistically downscaled vertical wind speed $w_{\mathrm{dsc},j}$ for use in Eq. 8 (the "aspect scheme"). $w_{\mathrm{dsc},j}$ is obtained by scaling the spatially averaged horizontal wind speed $\overline{vh}$ with the local downscaling factor $Y^{\mathrm{aspect}}_{\mathrm{dsc},j}$:

$$w_{\mathrm{dsc},j} = \overline{vh}\, Y^{\mathrm{aspect}}_{\mathrm{dsc},j}\, (\Delta\psi_j, \mu_j)\ . \tag{9}$$

$Y^{\mathrm{aspect}}_{\mathrm{dsc},j}$ is a function of μ_j and the local terrain aspect parameter $\Delta\psi_j$, defined as the local terrain aspect angle ψ_j relative to the low-resolution wind direction wd. $Y^{\mathrm{aspect}}\mathrm{dsc}, j$ was derived from the 3D wind simulation dataset over synthetic topographies:

$$Y^{\mathrm{aspect}}_{\mathrm{dsc}}(\Delta\psi, \mu) = [(\mathrm{a'} - \mathrm{b'}\, (\Delta\psi) + \mathrm{c'}\, \mathrm{erf}(\mathrm{d'}\, (\Delta\psi))]\, (\mathrm{e'} + \mu^{\mathrm{f'}})\ , \tag{10}$$

with constant parameters a' = -0.087122, b' = 0.4788, c' = 2.068, d' = 0.6298, e' = -0.046577 and f' = 0.72451. $w_{\mathrm{dsc},j}$ requires spatially averaged horizontal wind speed $\overline{vh}$, which we do not have available. We use a subgrid parameterization for the spatial mean horizontal wind speed vh_{sgp}, parameterizing the unresolved drag over topography by scaling low resolution horizontal wind speed vh with the subgrid sky view factor $F_{\mathrm{sky,sbg}}(L/\xi, \mu)$ (Helbig et al., 2017):

$$\overline{vh} = vh_{\mathrm{sgp}} = vh\, F_{\mathrm{sky,sbg}}(L/\xi, \mu)\ . \tag{11}$$

$F_{\mathrm{sky,sbg}}(L/\xi, \mu)$ is parameterized as in Helbig and Löwe (2014) and relies on domain size L, domain mean slope parameter $\overline{\mu}$ and terrain correlation length ξ in the domain. For further information on the PD model we refer to Helbig et al. (2024).

We calculated the HNW distribution based on PD on the same snow-off DSM as the terrain indices, and calculate each event in 1 hour time steps. Due to the locations of the measurement stations B1 and B2 we omit the sky view factor $F_{\mathrm{sky,sbg}}(L/\xi, \mu)$, when using these data as model input. The final HNWs are the accumulation of the fine-scale precipitation per computation step. We convert HNW PD to HN PD using Eq. 6 adapted with $\mathrm{HNW}^{\mathrm{PD}}_{j,\mathrm{E}}$. In Fig. 4 top right we show an example epoch of the terrain scaling parameter $X_{\mathrm{dsc},j}$ (Eq. 7), and scaled to HNW in the bottom row.

4 Results

4.1 Measurements of snow depth changes

We compute our reference for change of snow depths ΔHS, by subtracting the DSM at the start of an event, from the the DSM at the end of the event, using the DSMs derived from TLS measurements. Figure 5 shows ΔHS for the three selected main events and their sub-events. In the first event (E1) we recorded a mean increase in snow depth of 0.53 m, with a standard

https://doi.org/10.5194/egusphere-2026-485
Preprint. Discussion started: 13 February 2026

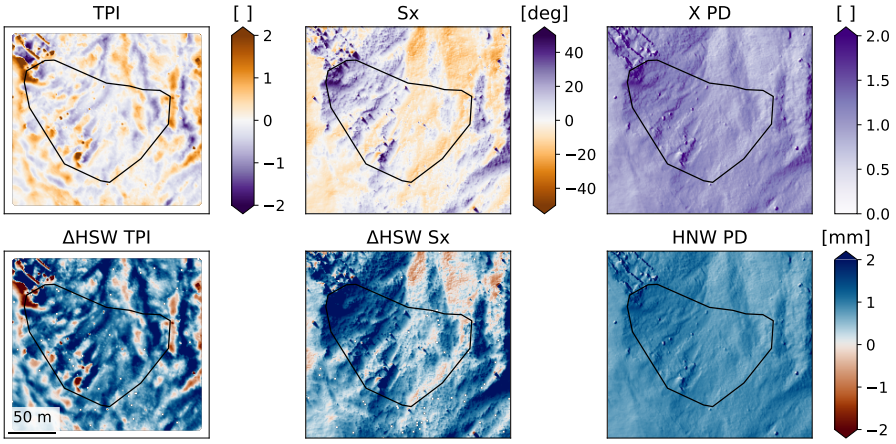

Figure 4. Terrain scaling parameters for the example epoch of 25 November 2023 21:00 - 22:00 UTC. TPI calculated with R of 10 m and Sx using D of 8 m, HNW icon 0.85 mm, mean wind speed of 5.2 m/s and wind direction of 315 deg. X PD corresponds to $X_{\mathrm{dsc},j}$ in Eq. 7. The extent of the figures correspond to the outline Ext in Fig. 1. For orientation, we plot the approximate outline of the TLS data as black polygon. For TPI we cropped a margin, due to artifacts caused by the spatial filter at the borders.

deviation over the measured area of 0.25 m in a time of 42 hours. The spatial distribution of new snow is varying, with up to 1.5 m snow accumulation in some areas, and no increase, or even a slight decrease in snow depth in other areas of 0.15 m. After the event of December 2023 (E2), we measured a mean increase in snow depth of 0.29 m, with a standard deviation of 0.26 m. The distribution pattern of snow depths is similar to E1. We find accumulations and depletions in similar areas, in both cases the prevailing wind direction during the event was north-west. The maximum accumulation of new snow is of a similar magnitude, but larger decreases occur. Several areas show a decrease in snow depth up to around -0.45 m, compared to before the event. In the last event of February 2024 (E3) the measured mean increase in snow depth is 0.37 m, with a standard deviation of 0.11 m. Due to the overall low wind speed during the event, we measured a rather homogeneous distribution of accumulated new snow without depletions.

4.2 Modelling snow depth distribution

Fig. 6 shows maps of the model results for the main events, and 7 shows an overview of the model results for all events and sub-events as probability density function. All results are masked by the pixels that are available from the TLS measurements. The spatial patterns of ΔHS TPI do not vary between the events, since TPI does only depend on the terrain and selected radius. In ΔHS Sx the spatial variations are different in each event, due to different wind directions. The PD model takes not only wind direction, but also wind speed into account. The difference between ΔHS Sx and HN PD are for example clearly visible in E3. ΔHS Sx accumulates the distributed $\overline{\mathrm{HNW}}$ of each epoch of wind directions with no further scaling, resulting in too much variation of snow depth distribution, where there is almost no variation resulting from the PD model.

https://doi.org/10.5194/egusphere-2026-485
Preprint. Discussion started: 13 February 2026

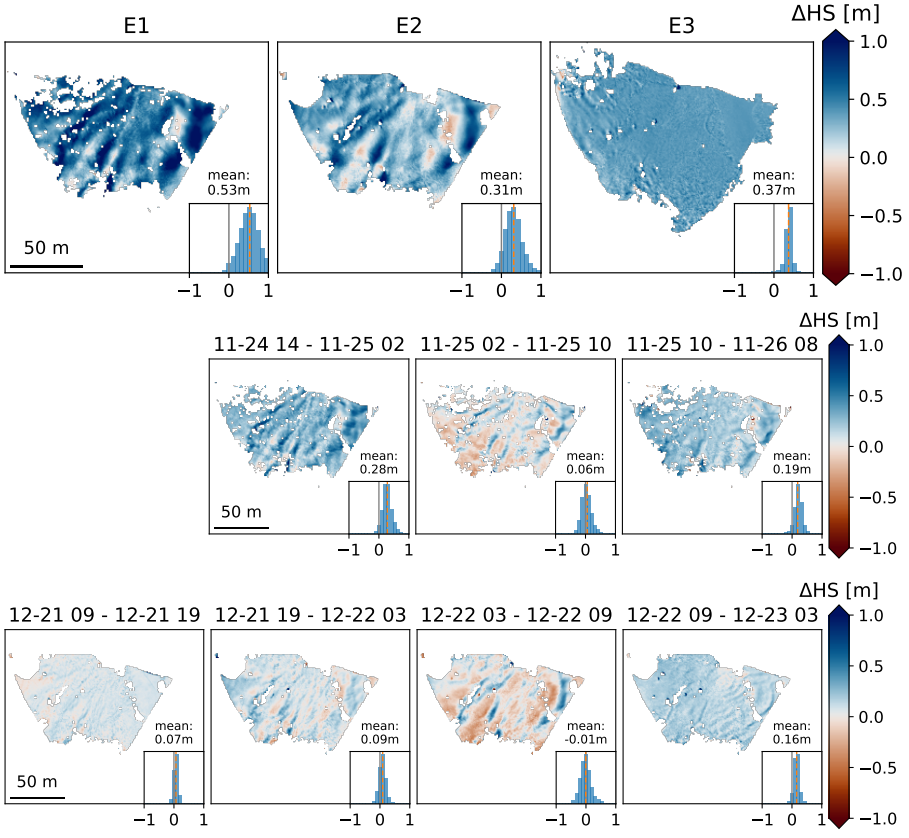

Figure 5. Measured change of snow depth ΔHS, calculated as the difference between the DSMs before and after the snowfall events and during the sub-events. Blue colours correspond to an increase of snow depth, and red colours to a decrease.

4.3 Model evaluation

In Fig. 8 we show the differences between the measured and the modelled ΔHSs and HNs. Generally, the mean differences indicate an underestimation of the modelled ΔHS and HNs, compared to ΔHS TLS, with exception of the TPI and PD model in E2. The error patterns are similar in the models for E1 and E2, underestimating areas with large, positive ΔHSs, and overestimating areas with small, or negative ΔHSs. In the case of E3, both ΔHS TPI and ΔHS Sx have large error distributions, but HN PD successfully represents the rather homogeneous snow depth distribution.

Figure 9 shows a comparison of the measured ΔHSs by TLS and modeled ΔHSs, using TPI, Sx and PD as scatter plots, with their Pearson and Spearman correlations coefficients (scatter plots for the sub-events are shown in the appendix Fig. A1 and A2). The highest correlations per event are achieved by the snow depths derived from terrain indices. The spatial correlations in E3 are very low for all methods. We point out the narrow distributions of ΔHS Sx in E2 and HN PD in E3. The ΔHS Sx distribution is influenced by the ratio of wind exposed to wind sheltered areas, while the HN PD distribution shows minimal

https://doi.org/10.5194/egusphere-2026-485
Preprint. Discussion started: 13 February 2026

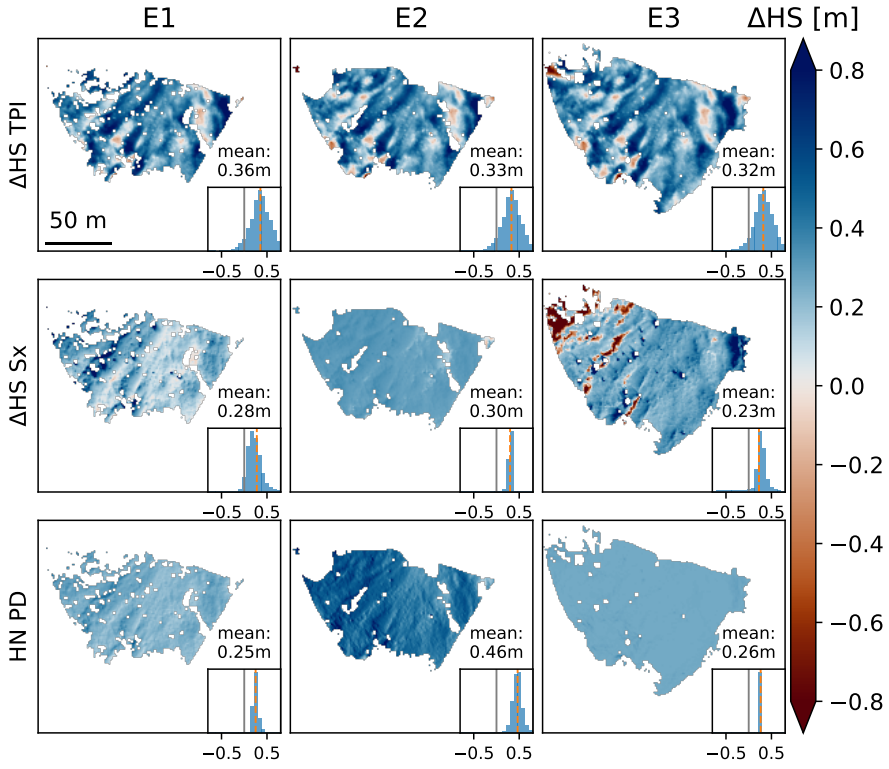

Figure 6. Spatial patterns of modelled ΔHS and HN. The results are masked by the spatial availability of TLS measurements. The grey line in the histogram corresponds to 0.0, and the orange dashed line shows the mean value.

variation in snow depths due to the low wind speeds during E3 and partially opposing wind directions during the event, which can even out the distribution of HN. Overall the correlations are moderate, with a generally higher value for the Spearman correlation, compared to Pearson. This suggests that there is no pure linear correlation.

In Table 2 we summarize all performance metrics of the models, compared to the measurements. The metrics for the sub-events are in the appendix (Tab. A1 and A2).

5 Discussion

5.1 Sensitivity to wind data

Wind plays an essential role in the pattern of snow depth distribution and many snow depth distribution models highly depend on the quality of wind field modelling. Also simple approaches, like the wind shelter index Sx rely on the wind direction, but the wind direction (and wind speeds) can vary significantly within small areas. In our measurement setup we have several wind measurements, each at a different topographic position. One station is located within the slope of release (B1), about

https://doi.org/10.5194/egusphere-2026-485
Preprint. Discussion started: 13 February 2026

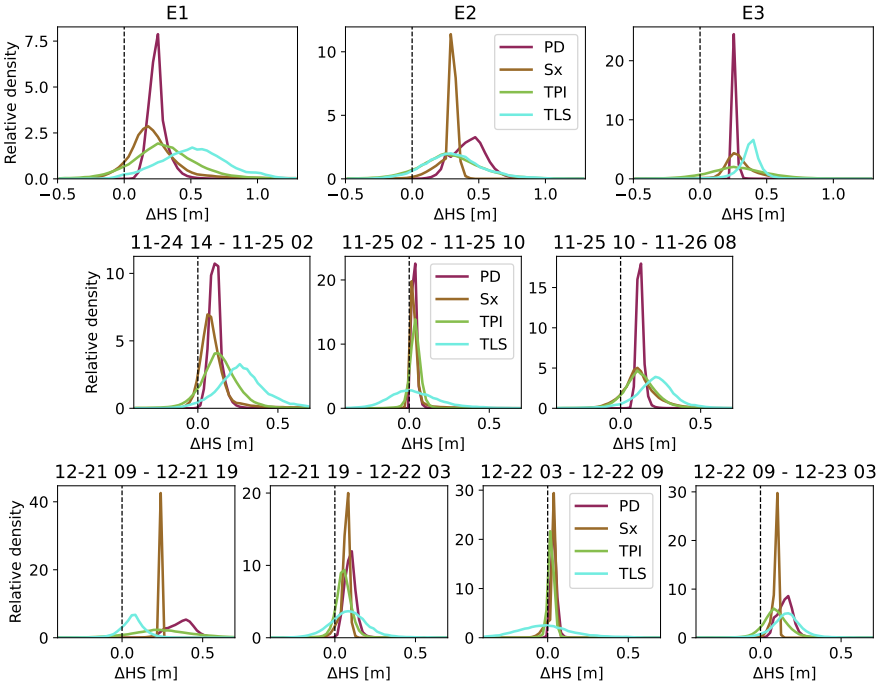

Figure 7. Probability density functions of measured and modelled ΔHS and HN for all events and sub-events. The legend entries PD, Sx and TPI refer to the modelled ΔHS or new snow HN, we use the shorter labels for better readability of the figure.

150 vertical meters below the local ridge line. The other station of our main test setup is installed on top of the monitored slope, on the local ridge (B2). Furthermore, we use the data of a station located on the mountain top of Braemabuehl (HFY). All stations are within a radius of about 700 m. This gives the possibility to assess the impact of different measurement locations. In Fig. 10 we show selected metrics for the PD and Sx model, with different data for wind input (speed and direction). For the mean and standard deviations we additionally show the values derived from the TLS measurements and the ICON model. In the Appendix (Fig. A3) we include an overview of the wind speed and direction data, for each evaluated event. The variations of mean HN PD are higher than for ΔHS Sx, as the PD model is also dependent on distributed wind speed, which is not considered in ΔHS Sx. The much higher standard deviations of ΔHS Sx in E3 stand out in this comparison. We attribute this to the applied scaling algorithm, which is currently not sensitive to wind speed. Among other things, we see a scaling more adaptive to wind speeds as an opportunity for improvement. There is no clear trend regarding the proximity of the wind station, it rather depends on the representativeness of the local wind patterns. For example, station B2 is very close to the evaluated slope, but the modelled results have often a higher correlation when using the wind data from ICON. With wind data from station B1 the correlations of the modelled and measured snow depths are mostly higher than the other wind inputs. These findings emphasize the importance of carefully selecting wind stations based on local wind patterns rather than just geographical proximity when planning and operating a monitoring system. In most regions, where the density of the measurement network is less dense than around our testsite, local wind measurements are sparse or not existing. In this context, gridded meteorological models

https://doi.org/10.5194/egusphere-2026-485
Preprint. Discussion started: 13 February 2026

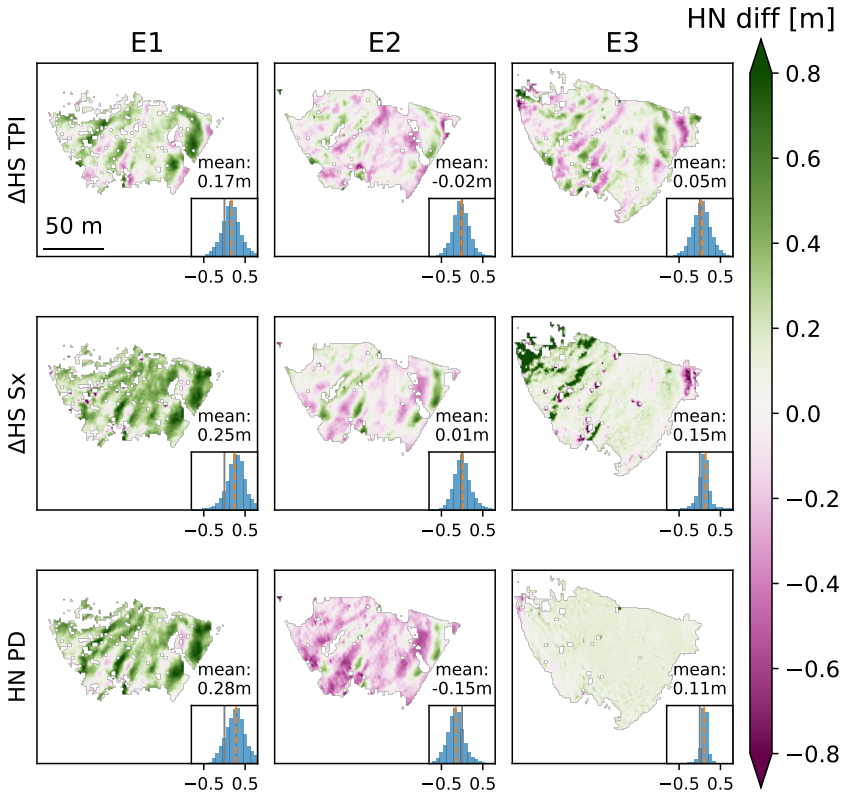

Figure 8. Differences of measured and modelled ΔHSs and HNs. Positive values (green colours) indicate an underestimation of the modelled ΔHSs, whereas negative values (pink) mean an overestimation of the modelled ΔHSs. In the histogram the grey line indicates the zero line and the dashed orange line corresponds to the mean of differences.

like ICON present a promising alternative, as they can provide consistent, high-resolution data in regions with limited or no measurement stations. However, the performance of ΔHS modelling using such models depends on how well the gridded data represents the local slope and wind patterns. Our results show that using gridded data is often comparable to using a nearby weather station, which possibly does not capture the local conditions of an evaluated slope.

5.2 Influence of underlying DSM

With the growth of the snowpack during winter, the terrain surface changes. If we want to predict an event of new snow distribution based on terrain features, the obvious would be to use the most recent DSM, which is however in most cases not available. With the DSM from 19 December 2023, we can compare the modelled results when using a snow-off DSM, or a more recent snow-covered DSM (Fig. 11) The results show that there is almost no difference in model performance. There is a slight decrease of RMSE and relative error (except for ΔHS Sx), and increase in Spearman correlation for ΔHS TPI, when using the more recent DSM, although the differences are very small. This is a valuable insight, since up-to-date DSM before snow fall

https://doi.org/10.5194/egusphere-2026-485
Preprint. Discussion started: 13 February 2026

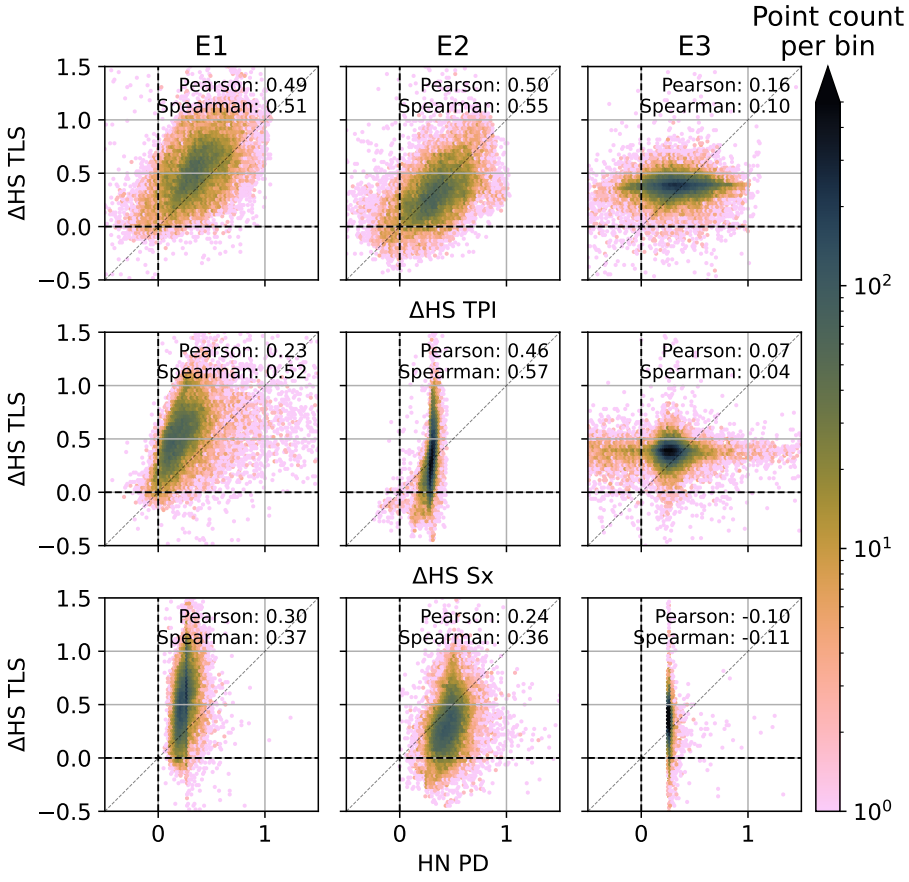

Figure 9. Scatter plots and Pearson and Spearman correlation coefficients of measured vs. modelled ΔHSs and HNs. Darker colours indicate a higher count per bin.

events are rarely available. However, we are aware that this result should be viewed with caution, as the extent of changes to the surface geometry depends strongly on the respective terrain features, the snow height and the snowpack conditions during each winter season.

5.3 Model applicability and limitations

In this study we tested the performance of various approaches to estimate the distribution of new snow or snow depth changes in an avalanche release area at very high temporal and spatial resolution. The simplest, most general approach is the use of topographic position index TPI. However, it depends only on one parameter, the radius of evaluation, which was here derived from its highest correlation with event averaged observed snow accumulation (Fig. 3). It is thus not sensitive to any wind variations in snowfall events. This is visible in Fig. 6, where the snow depth distribution pattern is the same for all events. There is only slight variation in scaling, according to the input of precipitation. This can be viewed as strength, as it makes

https://doi.org/10.5194/egusphere-2026-485
Preprint. Discussion started: 13 February 2026

Table 2. Performance measures for different models and meteorological events. As bias we calculated the mean of the differences between the TLS measurements and the model (see also Fig. 8), and the relative error refers to the median of relative errors. The best values per model are marked in bold numbers.

Model	Mean [m]	Std Dev [m]	RMSE [m]	Bias [m]	Rel. Error [%]	Pearson [ ]	Spearman [ ]
				E1			
TLS	0.47	0.25	-	-	-	-	-
TPI	0.36	0.23	**0.31**	**0.17**	**40**	**0.49**	0.51
Sx	0.28	0.36	0.47	0.25	63	0.23	**0.52**
PD	0.25	0.06	0.38	0.28	56	0.30	0.37
				E2			
TLS	0.29	0.26	-	-	-	-	-
TPI	0.33	0.24	0.23	-0.02	44	**0.50**	0.55
Sx	0.30	0.04	**0.22**	**0.01**	**38**	0.46	**0.57**
PD	0.46	0.13	0.28	-0.15	54	0.24	0.36
				E3			
TLS	0.37	0.11	-	-	-	-	-
TPI	0.32	0.24	0.25	**0.05**	39	**0.16**	0.10
Sx	0.23	0.67	0.69	0.15	36	0.07	0.04
PD	0.26	0.02	**0.16**	0.11	**33**	-0.10	**-0.11**

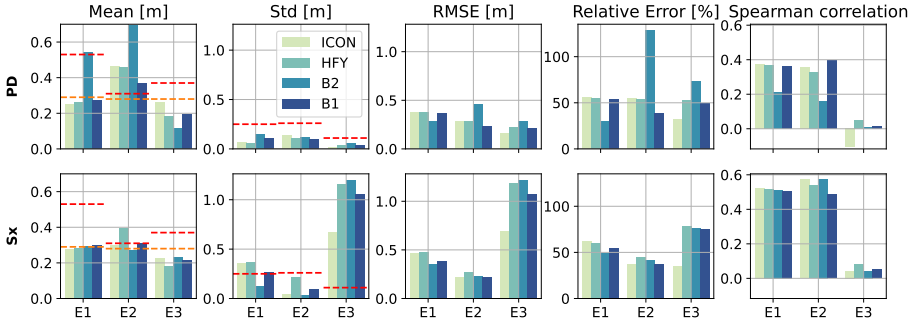

Figure 10. Metrics in comparison when using different wind input data for HN PD and Sx modelling. The mean and standard deviation (Std) refer to HN PD and Sx. The red and orange dashed lines correspond to the values derived from ΔHS TLS and HNW ICON ($\overline{\mathrm{HNW_E}}$ scaled by $\overline{\rho_\mathrm{E}}$). The error metrics RMSE, relative error and Spearman correlation refer to a comparison of HN PD and Sx to ΔHS TLS.

the model more generic which could be an advantage for mixed type events. However, it is also a limitation, because the distribution of ΔHS for preferential deposition or redistribution events strongly depends on the wind speed and wind direction and the approach using only the TPI can not be adapted to individual meteorological conditions (see e.g. event E3 Fig. 8).

https://doi.org/10.5194/egusphere-2026-485
Preprint. Discussion started: 13 February 2026

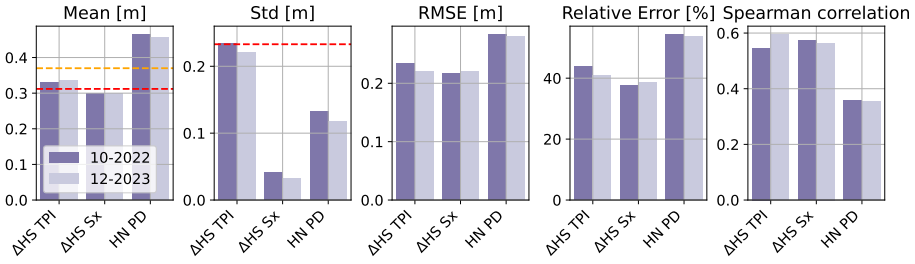

Figure 11. Metrics for HNs computed for E2, comparing the use of the snow-off DSM from 18 October 2022 (10-2022), or a more recent DSM with snow cover, in this case from 19 December 2023 (12-2023). The mean and standard deviation (Std) refer to ΔHS TPI, Sx and PD. The red and orange dashed lines correspond to the values derived from ΔHS TLS and HNW ICON ($\overline{\mathrm{HNW_E}}$ scaled by $\overline{\rho_\mathrm{E}}$). The error metrics RMSE, relative error and Spearman correlation refer to a comparison of ΔHS TPI, Sx, and PD to ΔHS TLS.

The wind shelter index Sx mainly depends on the wind direction, which makes it adaptable to different events, although the wind speeds are not considered. On this rather small evaluation area, the rescaling of both terrain indices to ΔHS strongly depends on the scaling method and the evaluated domain extent. This becomes evident for Sx in the example of E2, where there are only little areas that are wind exposed, so the scaling ratio becomes very small (α in Eq. 4 or Eq. 5), leading to very little variation of snow depths in the wind sheltered areas. In this study we use a scaling by mean and standard deviation, because when using the minimum and maximum (as suggested by e.g., Bavay and Egger (2014)) we saw almost no variations of ΔHS in our ROI, due to some large (or small) values in the evaluated extent of DSM. Another approach for improvement could be to link the scaling factor to wind speed. For example, the scaling factor leads to too much variation in ΔHS for E3, but it seems reasonable for E2, as wind speed and therefore ΔHS variability are greater there.

The presented model for HN based on PD takes all lacking parameters into account that are mentioned above, by relying on statistical downscaling of coarse meteorological parameters (precipitation, wind speed and direction). This allows an adaption to individual snowfall events, and the downscaling is designed to be broadly applicable, i.e., it is very little dependent on the resolution or extent of the model domain. However, the PD model has been developed for a spatial resolution of 30 m, and is the first time applied at the high resolution of 0.5 m. Currently, the statistical downscaling is based on Helbig et al. (2017) and Helbig et al. (2024). A point of improvement would be the use of more sophisticated modelling of very local wind fields, for example the use of machine learning models, that are able to model all three wind components. Ongoing work includes the adaptation of a versatile, deep-learning model Devine, proposed by Le Toumelin et al. (2023). As the model name suggests, the PD model is limited on the representation of the process of preferential deposition. In reality the distribution of new snow is always a combination of multiple processes, so especially with higher wind speeds when also snow redistribution occurs, or during warm periods impacting the snowpack, the model cannot describe the resulting snow distribution (see mixed and redistribution events in Fig. 7). For example, HN PD overestimates the absolute ΔHSs in E2. Given the rather high wind speeds as well as the warm period at the beginning of this event, other processes than preferential deposition, have likely contributed to shape the snow distribution during E2. However, since the model downscales coarse precipitation and coarse

https://doi.org/10.5194/egusphere-2026-485
Preprint. Discussion started: 13 February 2026

wind, the overestimation of HN could also be from inaccuracies in precipitation and wind input. The overall similar spatial bias pattern among the three models indicates that the distribution patterns agree, which suggests a possible improvement of the model performance by adjusting the absolute scaling to wind speed and precipitation. An explanation for the low spatial variability of HN in E3, calculated with the PD model, is the change of wind directions during the period of the event. Opposite wind directions with similar wind speeds can even out the accumulated result.

All presented models strongly depend on the input of precipitation ($\overline{\text{HNW}}$) and the scaling to ΔHS and HN, using the density ρ of new snow. In this study we use ρs, derived from manual, daily measurements of HN and HNW at the measurement site WFJ. For comparison, we derived ρs for the same evaluation periods from the automated weather station at WFJ, which is placed a few meters next to the manual measurement location. The correlation values do not change, since ρ is only a linear scaling factor, but we found variations in the bias of up to 0.18 m across the models and events, in comparison to ρ derived from the manual measurements.

A promising application of the presented models could be the spatio-temporal completion of TLS measured snow depth maps. In Fig. 12 we show a first attempt, where we show the TLS derived ΔHS, complemented with the ΔHSs modelled with TPI.

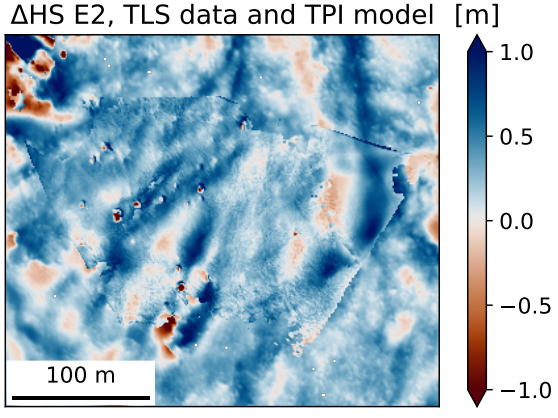

Figure 12. TLS data of E2 with gaps filled by the TPI model.

Our validation data is limited to a rather small area, due to the maximum measurement range of the TLS. Currently we use data from only one study site and evaluated three specific snowfall events. This has the consequence that we have only a certain variation of topography and meteorological conditions we can evaluate our models on. Furthermore, the measurements have local uncertainties in the range of 0.1–0.3 m (Ruttner et al., 2025), which has to be considered in the interpretation of error metrics.

https://doi.org/10.5194/egusphere-2026-485
Preprint. Discussion started: 13 February 2026

6 Conclusion and Outlook

The amount of new snow in an avalanche release area is crucial information for the prediction of avalanche danger, avalanche simulations, and applications like hazard indication mapping, where the accumulation of new snow is a factor in the definition of return periods (Bühler et al., 2022). Often, if at all, there are only snow depth measurements available from sparsely distributed flat field measurements, but no or little information within steep avalanche starting zones.

With our low-cost measurement setup we collect information on the snow depth distribution in an avalanche release area with high spatial and temporal resolution. Given weather- and line-of-sight-related gaps in the lidar data acquisition, we evaluated different model approaches for describing spatial changes in snow depth to complement observations and support applied use. Specifically, we tested low-complexity, terrain-based modelling approaches based on low input requirements and low computational demand. We tested approaches using the topographic position index TPI and wind shelter index Sx and a model for preferential deposition PD. Due to the differences in wind speeds and to air temperature in each event, we assume different leading processes that form the measured distribution of ΔHS. We found the highest correlations of measured and modelled ΔHSs, by applying a basic rescaling of the terrain indices TPI and Sx, for E1 and E2, being mixed events including snow redistribution. E3, being a preferential deposition event with low wind speeds, has a rather homogeneous ΔHS distribution, therefore we did not find clear correlations, but the best performance in terms of RMSE was achieved by the PD model. Overall the correlations are moderate (maximum Spearman of 0.57 for ΔHS Sx in E2), which indicates that we cannot fully explain the snow depth variability on such high spatio-temporal resolution using only terrain indices or statistical downscaling. For mixed events, the best approach in our results is ΔHS derived from the TPI, although it does not take into account the wind. The tested approaches which are considering the wind direction (Sx and PD model) would benefit from further optimisation and adaptation for high spatial resolutions of few meters, since they were originally developed for larger scales. We tested the PD and Sx model for the sensitivity to different input for wind data. Different wind data sources have a moderate impact on the model results, but with larger variations in the PD model results, which also takes wind speed into account. We could not derive a clear pattern of impact, for example regarding the proximity of the station to the test region. A better understanding of wind source impact on the model result will need further investigation. We also compared the results of ΔHS computations when using a snowfree- or more recent snow-covered DSM. The model performances are in most cases better on the snow-covered DSM, although the differences are small.

In the future, the evaluations could be strengthened by testing additional study sites (to cover a larger variety of topography), and a larger variety of snowfall events. The testing of a combination of the different model approaches could probably better capture the events. For example, a preferential deposition model can be applied for a basin scale prediction and then further downscaled on the slope scale at very fine resolutions using the TPI or Sx indices. Although we started more frequent data acquisitions with a promising measurement approach, snow depth distribution measurements from avalanche release areas with high spatial and temporal resolution are still very scarce. By further extending measurement setups at more locations and collecting relevant meteorological events, we can increase our understanding of avalanche formation processes and evaluate

https://doi.org/10.5194/egusphere-2026-485
Preprint. Discussion started: 13 February 2026

new modelling approaches. With more complete databases from avalanche release areas, machine learning models might also become a promising option for the future.

Code availability. Python code implementing the preferential deposition model described by Helbig et al. (2024) as used here is available from Helbig (2026). A python script for computing the relative terrain aspect parameter is available at Helbig (2023).

Author contributions. Study design: PR, NH and YB, Data processing: PR, with inputs from NH and AV, Manuscript: PR with contributions from all co-authors.

Competing interests. At least one of the (co-)authors is a member of the editorial board of The Cryosphere. The contact author has declared that none of the authors has any competing interests.

Acknowledgements. This research is funded by the Swiss National Science Foundation SNSF with the project "Avalanche Safety for Roads" (Nr. 207519). The authors want to thank Louis Quéno for fruitful discussions and help with the ICON dataset, the SLF workshop for the electronic design and operation of the measurement stations, as well as the community of Davos and SOS Jakobshorn for support and discussions regarding the test site.

https://doi.org/10.5194/egusphere-2026-485
Preprint. Discussion started: 13 February 2026

Appendix A: Appendix

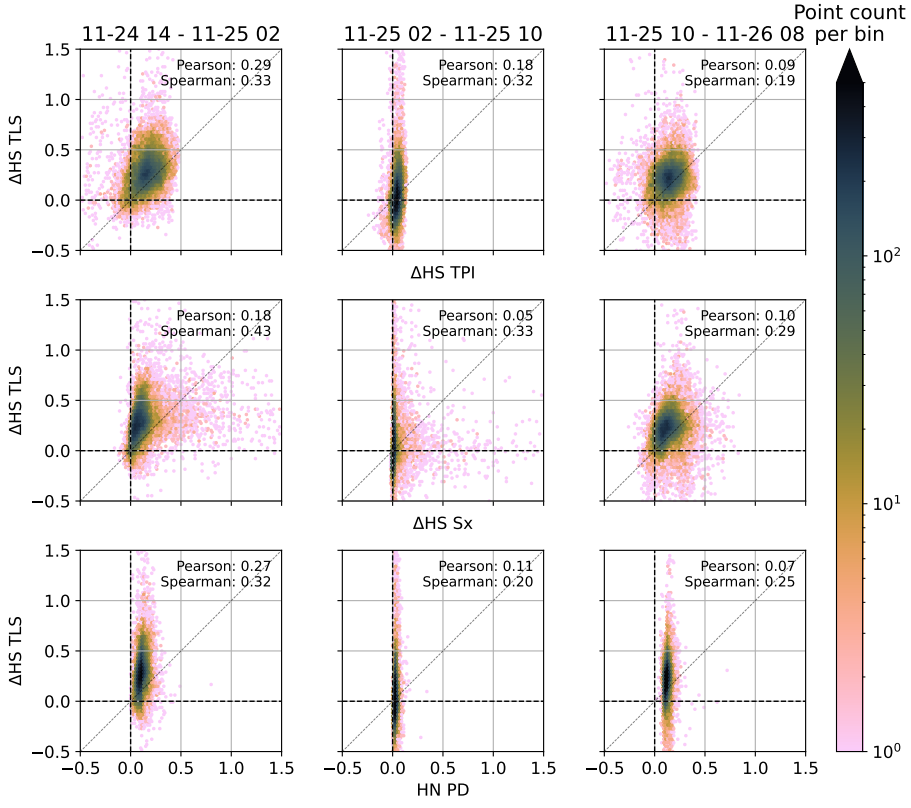

Figure A1. Scatter plots and Pearson and Spearman correlation coefficients of measured vs. modelled ΔHSs and HNs for sub events fo E1. Darker colours indicate a higher count per bin.

https://doi.org/10.5194/egusphere-2026-485
Preprint. Discussion started: 13 February 2026

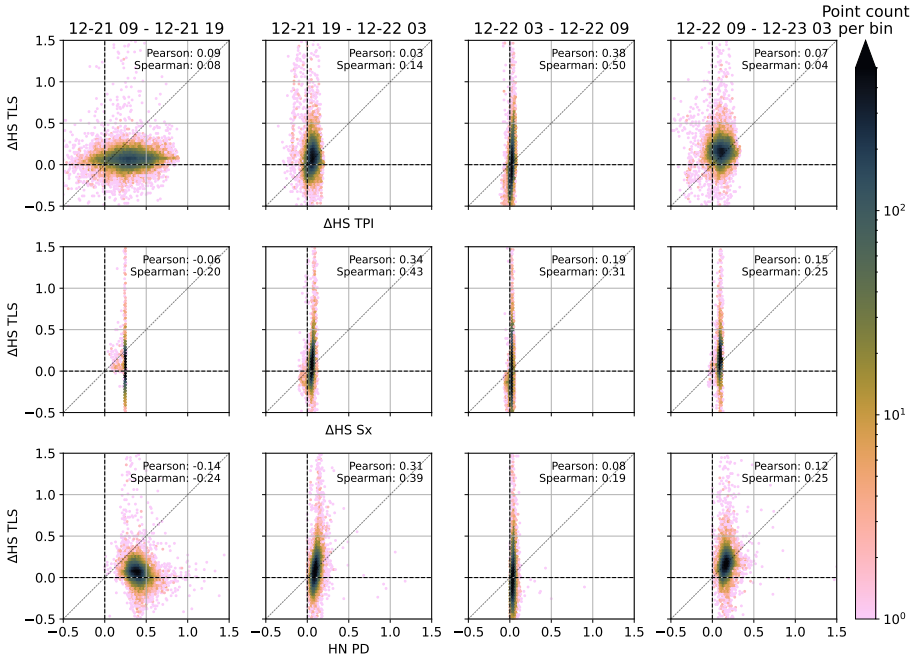

Figure A2. Scatter plots and Pearson and Spearman correlation coefficients of measured vs. modelled ΔHSs and HNs for sub events fo E2. Darker colours indicate a higher count per bin.

https://doi.org/10.5194/egusphere-2026-485
Preprint. Discussion started: 13 February 2026

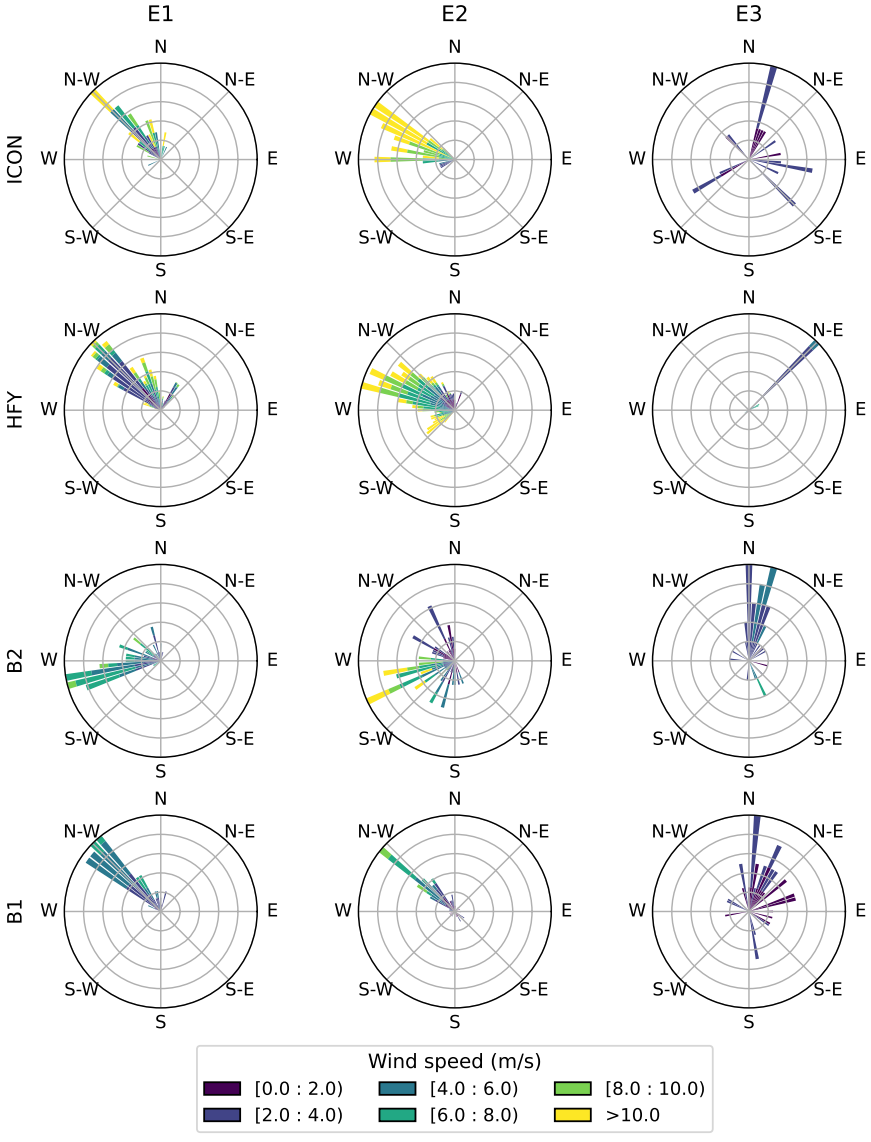

Figure A3. Overview of wind roses for events E1, E2, and E3, from the ICON model and measurement stations HFY, B2, and B1.

https://doi.org/10.5194/egusphere-2026-485
Preprint. Discussion started: 13 February 2026

Table A1. Performance measures for different models and meteorological events (sub-events of E1). As bias we calculated the mean of the differences between the TLS measurements and the model, and the relative error refers to the median of relative errors. The best values per model are marked in bold numbers.

Model	Mean [m]	Std Dev [m]	RMSE [m]	Bias [m]	Rel. Error [%]	Pearson [ ]	Spearman [ ]
12-21 09 – 12-21 19							
TLS	0.28	0.18	-	-	-	-	-
TPI	0.16	0.11	**0.21**	**0.12**	**49**	**0.29**	0.33
Sx	0.12	0.19	0.28	0.16	72	0.18	**0.43**
PD	0.11	0.03	0.24	0.17	64	0.27	0.32
12-21 19 – 12-22 03							
TLS	0.06	0.30	-	-	-	-	-
TPI	0.05	0.03	**0.29**	**0.01**	97	0.18	0.32
Sx	0.03	0.10	0.31	0.03	97	**0.05**	**0.33**
PD	0.03	0.01	0.30	0.03	**95**	0.11	0.20
12-22 03 – 12-22 09							
TLS	0.19	0.31	-	-	-	-	-
TPI	0.15	0.10	**0.32**	**0.04**	**50**	0.09	0.19
Sx	0.13	0.09	**0.32**	0.06	55	**0.10**	**0.29**
PD	0.12	0.02	**0.32**	0.06	51	0.07	0.25

https://doi.org/10.5194/egusphere-2026-485
Preprint. Discussion started: 13 February 2026

Table A2. Performance measures for different models and meteorological events (sub-events of E2). As bias we calculated the mean of the differences between the TLS measurements and the model, and the relative error refers to the median of relative errors. The best values per model are marked in bold numbers.

Model	Mean [m]	Std Dev [m]	RMSE [m]	Bias [m]	Rel. Error [%]	Pearson [ ]	Spearman [ ]
12-21 09 – 12-21 19							
TLS	0.07	0.12	-	-	-	-	-
TPI	0.29	0.20	0.32	-0.22	327	**0.09**	**0.08**
Sx	0.24	0.01	**0.21**	**-0.18**	**251**	-0.06	-0.20
PD	0.40	0.10	0.37	-0.33	448	-0.14	-0.24
12-21 19 – 12-22 03							
TLS	0.09	0.17	-	-	-	-	-
TPI	0.06	0.05	0.18	0.03	73	0.03	0.14
Sx	0.06	0.02	0.17	0.03	66	**0.34**	**0.43**
PD	0.10	0.03	**0.16**	**-0.01**	**58**	0.31	0.39
12-22 03 – 12-22 09							
TLS	-0.01	0.24	-	-	-	-	-
TPI	0.02	0.02	**0.23**	**-0.03**	**102**	**0.38**	**0.50**
Sx	0.03	0.01	0.24	**-0.03**	108	0.19	0.31
PD	0.04	0.02	0.24	-0.05	114	0.08	0.19
12-22 09 – 12-23 03							
TLS	0.16	0.17	-	-	-	-	-
TPI	0.11	0.08	0.19	0.05	53	0.07	0.04
Sx	0.10	0.01	0.18	0.06	49	**0.15**	**0.25**
PD	0.17	0.05	**0.17**	**-0.01**	**32**	0.12	**0.25**

https://doi.org/10.5194/egusphere-2026-485
Preprint. Discussion started: 13 February 2026

References

Adams, M. S., Gleirscher, E., Gigele, T., and Fromm, R.: Automated Terrestrial Laser Scanner measurements of small-scale snow avalanches, in: International Snow Science Workshop (ISSW) Proceedings 2013, Chamonix Mont-Blanc, France, p. 6, 2013.

Adams, M. S., Bühler, Y., and Fromm, R.: Multitemporal Accuracy and Precision Assessment of Unmanned Aerial System Photogrammetry for Slope-Scale Snow Depth Maps in Alpine Terrain, Pure and Applied Geophysics, 175, 3303–3324, https://doi.org/10.1007/s00024-017-1748-y, 2018.

Aksamit, N. O., Encinas-Bartos, A. P., Hancock, H., and Prokop, A.: Turbulent Snow Transport and Accumulation: New Reduced-Order Models and Diagnostics, https://eartharxiv.org/repository/view/9203/, 2025.

Baron, M., Haddjeri, A., Lafaysse, M., Le Toumelin, L., Vionnet, V., and Fructus, M.: SnowPappus v1.0, a blowing-snow model for large-scale applications of Crocus snow scheme, preprint, Cryosphere, https://doi.org/10.5194/gmd-2023-43, 2023.

Bavay, M. and Egger, T.: MeteoIO 2.4.2: a preprocessing library for meteorological data, Geoscientific Model Development, 7, 3135–3151, https://doi.org/10.5194/gmd-7-3135-2014, 2014.

Boardman, E. N., Fountain, A. G., Boardman, J. W., Painter, T. H., Burgess, E. W., Wilson, L., and Harpold, A. A.: Wind and topography underlie correlation between seasonal snowpack, mountain glaciers, and late-summer streamflow, The Cryosphere, 19, 3193–3225, https://doi.org/10.5194/tc-19-3193-2025, 2025.

Bühler, Y., Marty, M., Egli, L., Veitinger, J., Jonas, T., Thee, P., and Ginzler, C.: Snow depth mapping in high-alpine catchments using digital photogrammetry, The Cryosphere, 9, 229–243, https://doi.org/10.5194/tc-9-229-2015, 2015.

Bühler, Y., Adams, M. S., Bösch, R., and Stoffel, A.: Mapping snow depth in alpine terrain with unmanned aerial systems (UASs): potential and limitations, The Cryosphere, 10, 1075–1088, https://doi.org/10.5194/tc-10-1075-2016, 2016.

Bühler, Y., Bebi, P., Christen, M., Margreth, S., Stoffel, L., Stoffel, A., Marty, C., Schmucki, G., Caviezel, A., Kühne, R., Wohlwend, S., and Bartelt, P.: Automated avalanche hazard indication mapping on a statewide scale, Natural Hazards and Earth System Sciences, 22, 1825–1843, https://doi.org/10.5194/nhess-22-1825-2022, 2022.

Bührle, L. J., Marty, M., Eberhard, L. A., Stoffel, A., Hafner, E. D., and Bühler, Y.: Spatially continuous snow depth mapping by aeroplane photogrammetry for annual peak of winter from 2017 to 2021 in open areas, The Cryosphere, 17, 3383–3408, https://doi.org/10.5194/tc-17-3383-2023, 2023.

Dadic, R., Mott, R., Lehning, M., and Burlando, P.: Wind influence on snow depth distribution and accumulation over glaciers, Journal of Geophysical Research: Earth Surface, 115, https://doi.org/10.1029/2009JF001261, 2010.

Daudt, R. C., Wulf, H., Hafner, E. D., Bühler, Y., Schindler, K., and Wegner, J. D.: Snow depth estimation at country-scale with high spatial and temporal resolution, ISPRS Journal of Photogrammetry and Remote Sensing, 197, 105–121, https://doi.org/10.1016/j.isprsjprs.2023.01.017, 2023.

Deems, J. S., Painter, T. H., and Finnegan, D. C.: Lidar measurement of snow depth: a review, Journal of Glaciology, 59, 467–479, https://doi.org/10.3189/2013JoG12J154, 2013.

Deems, J. S., Gadomski, P. J., Vellone, D., Evanczyk, R., LeWinter, A. L., Birkeland, K. W., and Finnegan, D. C.: Mapping starting zone snow depth with a ground-based lidar to assist avalanche control and forecasting, Cold Regions Science and Technology, 120, 197–204, https://doi.org/10.1016/j.coldregions.2015.09.002, 2015.

Eberhard, L. A., Sirguey, P., Miller, A., Marty, M., Schindler, K., Stoffel, A., and Bühler, Y.: Intercomparison of photogrammetric platforms for spatially continuous snow depth mapping, The Cryosphere, 15, 69–94, https://doi.org/10.5194/tc-15-69-2021, 2021.

https://doi.org/10.5194/egusphere-2026-485
Preprint. Discussion started: 13 February 2026

Föhn, P. M. B. and Meister, R.: Distribution of Snow Drifts on Ridge Slopes: Measurements and Theoretical Approximations, Annals of Glaciology, 4, 52–57, https://doi.org/10.3189/S0260305500005231, 1983.

Gauer, P.: Numerical modeling of blowing and drifting snow in Alpine terrain, Journal of Glaciology, 47, 97–110, https://doi.org/10.3189/172756501781832476, 2001.

Gerber, F., Lehning, M., Hoch, S. W., and Mott, R.: A close-ridge small-scale atmospheric flow field and its influence on snow accumulation, Journal of Geophysical Research: Atmospheres, 122, 7737–7754, https://doi.org/10.1002/2016JD026258, 2017.

Goelles, T., Wallner, S., Schlager, B., Prokop, A., Gaisberger, C., Schratter, M., and Muckenhuber, S.: Low-Cost lidar as an Easy-to-Use REST API: Permanently Installed Systems for Cryospheric Research and Beyond, pp. EGU25–14 949, https://doi.org/10.5194/egusphere-egu25-14949, 2025.

Groot Zwaaftink, C. D., Mott, R., and Lehning, M.: Seasonal simulation of drifting snow sublimation in Alpine terrain, Water Resour. Res., 49, 1581–1590, https://doi.org/10.1002/wrcr.20137, 2013.

Grünewald, T. and Lehning, M.: Are flat-field snow depth measurements representative? A comparison of selected index sites with areal snow depth measurements at the small catchment scale, Hydrological Processes, 29, 1717–1728, https://doi.org/10.1002/hyp.10295, 2015.

Grünewald, T., Schirmer, M., Mott, R., and Lehning, M.: Spatial and temporal variability of snow depth and ablation rates in a small mountain catchment, The Cryosphere, 4, 215–225, https://doi.org/10.5194/tc-4-215-2010, 2010.

Grünewald, T., Stötter, J., Pomeroy, J. W., Dadic, R., Moreno Baños, I., Marturià, J., Spross, M., Hopkinson, C., Burlando, P., and Lehning, M.: Statistical modelling of the snow depth distribution in open alpine terrain, Hydrology and Earth System Sciences, 17, 3005–3021, https://doi.org/10.5194/hess-17-3005-2013, 2013.

Hames, O., Jafari, M., Wagner, D. N., Raphael, I., Clemens-Sewall, D., Polashenski, C., Shupe, M. D., Schneebeli, M., and Lehning, M.: Modeling the small-scale deposition of snow onto structured Arctic sea ice during a MOSAiC storm using snowBedFoam 1.0., Geoscientific Model Development, 15, 6429–6449, https://doi.org/10.5194/gmd-15-6429-2022, 2022.

Helbig, N.: Snowfall downscaling Source code to calculate the relative terrain aspect parameter, https://doi.org/http://dx.doi.org/10.16904/envidat.435, 2023.

Helbig, N.: Source code for a preferential snowfall deposition model, https://doi.org/http://dx.doi.org/10.16904/envidat.725, 2026.

Helbig, N. and Löwe, H.: Parameterization of the spatially averaged sky view factor in complex topography, Journal of Geophysical Research: Atmospheres, 119, 4616–4625, https://doi.org/10.1002/2013JD020892, 2014.

Helbig, N., van Herwijnen, A., Magnusson, J., and Jonas, T.: Fractional snow-covered area parameterization over complex topography, Hydrol. Earth Syst. Sci., 19, 1339–1351, https://doi.org/10.5194/hess-19-1339-2015, 2015.

Helbig, N., Mott, R., van Herwijnen, A., Winstral, A., and Jonas, T.: Parameterizing surface wind speed over complex topography, Journal of Geophysical Research: Atmospheres, 122, 651–667, https://doi.org/10.1002/2016JD025593, 2017.

Helbig, N., Bühler, Y., Eberhard, L., Deschamps-Berger, C., Gascoin, S., Dumont, M., Revuelto, J., Deems, J. S., and Jonas, T.: Fractional snow-covered area: scale-independent peak of winter parameterization, The Cryosphere, 15, 615–632, https://doi.org/10.5194/tc-15-615-2021, 2021.

Helbig, N., Mott, R., Bühler, Y., Le Toumelin, L., and Lehning, M.: Snowfall deposition in mountainous terrain: a statistical downscaling scheme from high-resolution model data on simulated topographies, Frontiers in Earth Science, 11, https://doi.org/10.3389/feart.2023.1308269, 2024.

Holfuy: Holfuy, https://holfuy.com, last accessed: 2025-11-27, 2025.

https://doi.org/10.5194/egusphere-2026-485
Preprint. Discussion started: 13 February 2026

Le Toumelin, L., Gouttevin, I., Helbig, N., Galiez, C., Roux, M., and Karbou, F.: Emulating the Adaptation of Wind Fields to Complex Terrain with Deep Learning, Artificial Intelligence for the Earth Systems, 2, https://doi.org/10.1175/AIES-D-22-0034.1, 2023.

Lehning, M. and Fierz, C.: Assessment of snow transport in avalanche terrain, Cold Regions Science and Technology, 51, 240–252, https://doi.org/10.1016/j.coldregions.2007.05.012, 2008.

Lehning, M., Völksch, I., Gustafsson, D., Nguyen, T. A., Stähli, M., and Zappa, M.: ALPINE3D: a detailed model of mountain surface processes and its application to snow hydrology, Hydrological Processes, 20, 2111–2128, https://doi.org/10.1002/hyp.6204, 2006.

Lehning, M., Löwe, H., Ryser, M., and Raderschall, N.: Inhomogeneous precipitation distribution and snow transport in steep terrain, Water Resour. Res., 44, https://doi.org/10.1029/2007WR006545, 2008.

Lehning, M., Grünewald, T., and Schirmer, M.: Mountain snow distribution governed by an altitudinal gradient and terrain roughness, Geophysical Research Letters, 38, https://doi.org/10.1029/2011GL048927, 2011.

Li, G., Wang, Z. S., and Huang, N.: A Snow Distribution Model Based on Snowfall and Snow Drifting Simulations in Mountain Area, Journal of Geophysical Research: Atmospheres, 123, 7193–7203, https://doi.org/10.1029/2018JD028434, 2018.

Li, L. and Pomeroy, J. W.: Estimates of Threshold Wind Speeds for Snow Transport Using Meteorological Data, Journal of Applied Meteorology and Climatology, 36, 205–213, https://doi.org/10.1175/1520-0450(1997)036<0205:EOTWSF>2.0.CO;2, 1997.

Liston, G. E. and Sturm, M.: A snow-transport model for complex terrain, Journal of Glaciology, 44, 498–516, https://doi.org/10.3189/S0022143000002021, 1998.

López-Moreno, J. I., Revuelto, J., Alonso-González, E., Sanmiguel-Vallelado, A., Fassnacht, S. R., Deems, J., and Morán-Tejeda, E.: Using very long-range terrestrial laser scanner to analyze the temporal consistency of the snowpack distribution in a high mountain environment, Journal of Mountain Science, 14, 823–842, https://doi.org/10.1007/s11629-016-4086-0, 2017.

Meloche, J., Langlois, A., Rutter, N., McLennan, D., Royer, A., Billecocq, P., and Ponomarenko, S.: High-resolution snow depth prediction using Random Forest algorithm with topographic parameters: A case study in the Greiner watershed, Nunavut, Hydrological Processes, 36, e14 546, https://doi.org/10.1002/hyp.14546, 2022.

Melvold, K. and Skaugen, T.: Multiscale spatial variability of lidar-derived and modeled snow depth on Hardangervidda, Norway, Annals of Glaciology, 54, 273–281, https://doi.org/10.3189/2013AoG62A161, 2013.

Meyer, J., Deems, J. S., Bormann, K. J., Shean, D. E., and Skiles, S. M.: Mapping snow depth and volume at the alpine watershed scale from aerial imagery using Structure from Motion, Frontiers in Earth Science, 10, https://doi.org/10.3389/feart.2022.989792, 2022.

Nolan, M., Larsen, C., and Sturm, M.: Mapping snow depth from manned aircraft on landscape scales at centimeter resolution using structure-from-motion photogrammetry, The Cryosphere, 9, 1445–1463, https://doi.org/10.5194/tc-9-1445-2015, 2015.

Pielmeier, C., Zweifel, B., Techel, F., Marty, C., Grüter, S., and Stucki, T.: Schnee und Lawinen in den Schweizer Alpen, vol. 145 of *WSL Berichte*, Swiss Federal Institute for Forest, Snow and Landscape Research, WSL, https://doi.org/10.55419/wsl:36046, 2024.

Prokop, A.: Assessing the applicability of terrestrial laser scanning for spatial snow depth measurements, Cold Regions Science and Technology, 54, 155–163, https://doi.org/10.1016/j.coldregions.2008.07.002, 2008.

Prokop, A., Schön, P., Vionnet, V., Naaim-Bouvet, F., Guyomarc'H, G., Durand, Y., Bellot, H., Singer, F., and Nishimura, K.: A comparison of terrain-based parameter, wind-field modelling and TLS snow depth data for snow drift modelling, in: International Snow Science Workshop (ISSW), International Snow Science Workshop (ISSW 2013), Grenoble Chamonix-Mont-Blanc, France, October 7-11, 2013 : a merging of theory and practice. Florence Naaim-Bouvet, Yves Durand, Richard Lambert (ed.), pp. p. 108 – p. 113, Irstea, ANENA, Meteo France, Grenoble - Chamonix Mont-Blanc, France, https://hal.science/hal-00949745, 2013.

https://doi.org/10.5194/egusphere-2026-485
Preprint. Discussion started: 13 February 2026

Quéno, L., Mott, R., Morin, P., Cluzet, B., Mazzotti, G., and Jonas, T.: Snow redistribution in an intermediate-complexity snow hydrology modelling framework, The Cryosphere, 18, 3533–3557, https://doi.org/10.5194/tc-18-3533-2024, 2024.

Revuelto, J., López-Moreno, J. I., Azorin-Molina, C., Zabalza, J., Arguedas, G., and Vicente-Serrano, S. M.: Mapping the annual evolution of snow depth in a small catchment in the Pyrenees using the long-range terrestrial laser scanning, Journal of Maps, https://www.tandfonline.com/doi/abs/10.1080/17445647.2013.869268, 2014.

Revuelto, J., Billecocq, P., Tuzet, F., Cluzet, B., Lamare, M., Larue, F., and Dumont, M.: Random forests as a tool to understand the snow depth distribution and its evolution in mountain areas, Hydrol. Process., 34, 5384–5401, https://doi.org/https://doi.org/10.1002/hyp.13951, 2020a.

Revuelto, J., Billecocq, P., Tuzet, F., Cluzet, B., Lamare, M., Larue, F., and Dumont, M.: Random forests as a tool to understand the snow depth distribution and its evolution in mountain areas, Hydrological Processes, 34, 5384–5401, https://doi.org/10.1002/hyp.13951, 2020b.

Ruttner, P., Voordendag, A., Hartmann, T., Glaus, J., Wieser, A., and Bühler, Y.: Monitoring snow depth variations in an avalanche release area using low-cost lidar and optical sensors, Natural Hazards and Earth System Sciences, 25, 1315–1330, https://doi.org/10.5194/nhess-25-1315-2025, 2025.

Saigger, M., Sauter, T., Schmid, C., Collier, E., Goger, B., Kaser, G., Prinz, R., Voordendag, A., and Mölg, T.: A Drifting and Blowing Snow Scheme in the Weather Research and Forecasting Model, Journal of Advances in Modeling Earth Systems, 16, https://doi.org/https://doi.org/10.1029/2023MS004007, 2024.

Schirmer, M., Wirz, V., Clifton, A., and Lehning, M.: Persistence in intra-annual snow depth distribution: 1. Measurements and topographic control, Water Resources Research, 47, https://doi.org/10.1029/2010WR009426, 2011.

Schneiderbauer, S. and Prokop, A.: The atmospheric snow-transport model: SnowDrift3D, Journal of Glaciology, 57, 526–542, https://doi.org/10.3189/002214311796905677, 2011.

Schweizer, J., Bruce Jamieson, J., and Schneebeli, M.: Snow avalanche formation, Reviews of Geophysics, 41, https://doi.org/10.1029/2002RG000123, 2003.

Schön, P., Prokop, A., Vionnet, V., Guyomarc'h, G., Naaim-Bouvet, F., and Heiser, M.: Improving a terrain-based parameter for the assessment of snow depths with TLS data in the Col du Lac Blanc area, Cold Regions Science and Technology, 114, 15–26, https://doi.org/10.1016/j.coldregions.2015.02.005, 2015.

Skaugen, T.: Modelling the spatial variability of snow water equivalent at the catchment scale, Hydrology and Earth System Sciences, 11, 1543–1550, https://doi.org/10.5194/hess-11-1543-2007, 2007.

Skaugen, T. and Melvold, K.: Modeling the snow depth variability with a high-resolution lidar data set and nonlinear terrain dependency, Water Resour. Res., 55, 9689–9704, https://doi.org/10.1029/2019WR025030, 2019.

Vander Jagt, B., Lucieer, A., Wallace, L., Turner, D., and Durand, M.: Snow Depth Retrieval with UAS Using Photogrammetric Techniques, Geosciences, 5, 264–285, https://doi.org/10.3390/geosciences5030264, 2015.

Vionnet, V., Martin, E., Masson, V., Guyomarc'h, G., Naaim-Bouvet, F., Prokop, A., Durand, Y., and Lac, C.: Simulation of wind-induced snow transport and sublimation in alpine terrain using a fully coupled snowpack/atmosphere model, The Cryosphere, 8, 395–415, https://doi.org/10.5194/tc-8-395-2014, 2014.

Vionnet, V., Marsh, C. B., Menounos, B., Gascoin, S., Wayand, N. E., Shea, J., Mukherjee, K., and Pomeroy, J. W.: Multi-scale snowdrift-permitting modelling of mountain snowpack, The Cryosphere, 15, 743–769, https://doi.org/10.5194/tc-15-743-2021, 2021.

https://doi.org/10.5194/egusphere-2026-485
Preprint. Discussion started: 13 February 2026

Voordendag, A., Goger, B., Prinz, R., Sauter, T., Mölg, T., Saigger, M., and Kaser, G.: A novel framework to investigate wind-driven snow redistribution over an Alpine glacier: combination of high-resolution terrestrial laser scans and large-eddy simulations, The Cryosphere, 18, 849–868, https://doi.org/10.5194/tc-18-849-2024, 2024.

Wang, Z. and Huang, N.: Numerical simulation of the falling snow deposition over complex terrain, Journal of Geophysical Research: Atmospheres, 122, 980–1000, https://doi.org/10.1002/2016JD025316, 2017.

Weiss, A.: Topographic position and landforms analysis, in: Poster presentation, ESRI user conference, San Diego, CA, vol. 200, 2001.

Winstral, A. and Marks, D.: Simulating wind fields and snow redistribution using terrain-based parameters to model snow accumulation and melt over a semi-arid mountain catchment, Hydrological Processes, 16, 3585–3603, https://doi.org/10.1002/hyp.1238, 2002.

Winstral, A., Elder, K., and Davis, R. E.: Spatial Snow Modeling of Wind-Redistributed Snow Using Terrain-Based Parameters, Journal of Hydrometeorology, 3, 524–538, https://doi.org/10.1175/1525-7541(2002)003<0524:SSMOWR>2.0.CO;2, 2002.

Wiscombe, W. J. and Warren, S. G.: A Model for the Spectral Albedo of Snow. I: Pure Snow, Journal of the Atmospheric Sciences, 37, 2712–2733, https://doi.org/10.1175/1520-0469(1980)037<2712:AMFTSA>2.0.CO;2, 1980.

Zängl, G., Reinert, D., Rípodas, P., and Baldauf, M.: The ICON (ICOsahedral Non-hydrostatic) modelling framework of DWD and MPI-M: Description of the non-hydrostatic dynamical core, Quarterly Journal of the Royal Meteorological Society, 141, 563–579, https://doi.org/10.1002/qj.2378, 2015.